Research Article | Vol. 25, No. 9 | 1 May 2017 | OPTICS EXPRESS 10177

Optics EXPRESS

Terahertz generation mechanism in nano-grating electrode photomixers on Fe-doped InGaAsP

RESHMA A. MOHANDAS,[1,4] JOSHUA R. FREEMAN,[1,*] MICHELE NATRELLA,[2] MARK C. ROSAMOND,[1] LALITHA PONNAMPALAM,[2] MARTYN J. FICE,[2] ALWYN J. SEEDS,[2] PAUL. J. CANNARD,[3] MICHAEL. J. ROBERTSON,[3] DAVID. G. MOODIE,[3] A. GILES DAVIES,[1] EDMUND H. LINFIELD,[1] AND PAUL DEAN[1]

[1]*Institute of Microwaves & Photonics, University of Leeds, Leeds, LS2 9JT, UK*
[2]*Department of Electronic and Electrical Engineering, University College London, London, WC1E 7JE, UK*
[3]*CIP Technologies, Adastral Park, Martlesham Heath, Ipswich, Suffolk, IP5 3RE, UK*
[4]*eenra@leeds.ac.uk*
[*]*j.r.freeman@leeds.ac.uk*

Abstract: We report the generation mechanism associated with nano-grating electrode photomixers fabricated on Fe-doped InGaAsP substrates. Two different emitter designs incorporating nano-gratings coupled to the same broadband antenna were characterized in a continuous-wave terahertz (THz) frequency system employing telecommunications wavelength lasers for generation and coherent detection. The current-voltage characteristics and THz emission bandwidth of the emitters is compared for different bias polarities and optical polarisations. The THz output from the emitters is also mapped as a function of the position of the laser excitation spot for both continuous-wave and pulsed excitation. This mapping, together with full-wave simulations of the structures, confirms the generation mechanism to be due to an enhanced optical electric field at the grating tips resulting in increased optical absorption, coinciding with a concentration of the electrostatic field.

OCIS codes: (040.2235) Far infrared or terahertz; (160.5140) Photoconductive materials; (140.5960) Semiconductor lasers; (310.6628) Subwavelength structures, nanostructures.

References and links

1. J. Kröll, J. Darmo, S. S. Dhillon, X. Marcadet, M. Calligaro, C. Sirtori, and K. Unterrainer, "Phase-resolved measurements of stimulated emission in a laser," Nature **449**(7163), 698–701 (2007).
2. M. Tonouchi, "Cutting-edge terahertz technology," Nat. Photonics **1**(2), 97–105 (2007).
3. B. Ferguson and X.-C. Zhang, "Materials for terahertz science and technology," Nat. Mater. **1**(1), 26–33 (2002).
4. T. Ouchi, K. Kajiki, T. Koizumi, T. Itsuji, Y. Koyama, R. Sekiguchi, O. Kubota, and K. Kawase, "Terahertz imaging system for medical applications and related high efficiency terahertz devices," J. Infrared Millim. Terahertz Waves **35**(1), 118–130 (2014).
5. K. Kawase, Y. Ogawa, Y. Watanabe, and H. Inoue, "Non-destructive terahertz imaging of illicit drugs using spectral fingerprints," Opt. Express **11**(20), 2549–2554 (2003).
6. N. Karpowicz, H. Zhong, C. Zhang, K.-I. Lin, J.-S. Hwang, J. Xu, and X. C. Zhang, "Compact continuous-wave subterahertz system for inspection applications," Appl. Phys. Lett. **86**(5), 054105 (2005).
7. S. Bartalini, L. Consolino, P. Cancio, P. De Natale, P. Bartolini, A. Taschin, M. De Pas, H. Beere, D. Ritchie, M. S. Vitiello, and R. Torre, "Frequency-comb-assisted terahertz quantum cascade laser spectroscopy," Phys. Rev. X **4**(2), 021006 (2014).
8. E. Castro-Camus and M. Alfaro, "Photoconductive devices for terahertz pulsed spectroscopy: a review [Invited]," Photonics Res. **4**(3), A36–A42 (2016).
9. I. S. Gregory, W. R. Tribe, B. E. Cole, C. Baker, M. J. Evans, I. V. Bradley, E. H. Linfield, A. G. Davies, and M. Missous, "Phase sensitive continuous-wave THz imaging using diode lasers," Electron. Lett. **40**(2), 143–145 (2004).

#285807 https://doi.org/10.1364/OE.25.010177
Journal © 2017 Received 1 Feb 2017; revised 27 Mar 2017; accepted 27 Mar 2017; published 25 Apr 2017

Optics EXPRESS

10. N. Karpowicz, H. Zhong, J. Xu, K.-I. Lin, J.-S. Hwang, and X.-C. Zhang, "Comparison between pulsed terahertz time-domain imaging and continuous wave terahertz imaging," Semicond. Sci. Technol. **20**(7), S293–S299 (2005).
11. S. Preu, G. H. Dohler, S. Malzer, L. J. Wang, and A. C. Gossard, "Tunable, continuous-wave Terahertz photomixer sources and applications," J. Appl. Phys. **109**(6), 061301 (2011).
12. S. Verghese, K. A. McIntosh, S. Calawa, W. F. DiNatale, E. K. Duerr, and K. A. Molvar, "Generation and detection of coherent terahertz waves using two photomixers," Appl. Phys. Lett. **73**(26), 3824–3826 (1998).
13. S. Verghese, K. A. McIntosh, and E. R. Brown, "Highly tunable fiber-coupled photomixers with coherent terahertz output power," IEEE Trans. Microw. Theory Tech. **45**(8), 1301–1309 (1997).
14. E. R. Brown, K. A. McIntosh, F. W. Smith, K. B. Nichols, M. J. Manfra, C. L. Dennis, and J. P. Mattia, "Milliwatt output levels and superquadratic bias dependence in a low-temperature-grown GaAs photomixer," Appl. Phys. Lett. **64**(24), 3311–3313 (1994).
15. S. M. Duffy, S. Verghese, K. A. McIntosh, A. Jackson, A. C. Gossard, and S. Matsuura, "Accurate modeling of dual dipole and slot elements used with photomixers for coherent terahertz output power," IEEE Trans. Microw. Theory Tech. **49**(6), 1032–1038 (2001).
16. J. Mangeney, A. Merigault, N. Zerounian, P. Crozat, K. Blary, and J. F. Lampin, "Continuous wave terahertz generation up to 2THz by photomixing on ion-irradiated In0.53Ga0.47As at 1.55μm wavelengths," Appl. Phys. Lett. **91**(24), 241102 (2007).
17. R. A. Mohandas, J. R. Freeman, M. C. Rosamond, O. Hatem, S. Chowdhury, L. Ponnampalam, M. Fice, A. J. Seeds, P. J. Cannard, M. J. Robertson, D. G. Moodie, J. E. Cunningham, A. G. Davies, E. H. Linfield, and P. Dean, "Generation of continuous wave terahertz frequency radiation from metal-organic chemical vapour deposition grown Fe-doped InGaAs and InGaAsP," J. Appl. Phys. **119**(15), 153103 (2016).
18. C. W. Berry, N. Wang, M. R. Hashemi, M. Unlu, and M. Jarrahi, "Significant performance enhancement in photoconductive terahertz optoelectronics by incorporating plasmonic contact electrodes," Nat. Commun. **4**, 1622 (2013).
19. C. W. Berry, M. R. Hashemi, S. Preu, H. Lu, A. C. Gossard, and M. Jarrahi, "High power terahertz generation using 1550 nm plasmonic photomixers," Appl. Phys. Lett. **105**(1), 011121 (2014).
20. S. H. Yang, R. Watts, X. Li, N. Wang, V. Cojocaru, J. O'Gorman, L. P. Barry, and M. Jarrahi, "Tunable terahertz wave generation through a bimodal laser diode and plasmonic photomixer," Opt. Express **23**(24), 31206–31215 (2015).
21. S.-H. Yang and M. Jarrahi, "Frequency-tunable continuous-wave terahertz sources based on GaAs plasmonic photomixers," Appl. Phys. Lett. **107**(13), 131111 (2015).
22. H. Tanoto, J. H. Teng, Q. Y. Wu, M. Sun, Z. N. Chen, S. A. Maier, B. Wang, C. C. Chum, G. Y. Si, A. J. Danner, and S. J. Chua, "Nano-antenna in a photoconductive photomixer for highly efficient continuous wave terahertz emission," Sci. Rep. **3**, 2824 (2013).
23. C. W. Berry and M. Jarrahi, "Terahertz generation using plasmonic photoconductive gratings," New J. Phys. **14**(10), 105029 (2012).
24. E. R. Brown, F. W. Smith, and K. A. McIntosh, "Coherent millimeter-wave generation by heterodyne conversion in low-temperature-grown GaAs photoconductors," J. Appl. Phys. **73**(3), 1480–1484 (1993).
25. Y. Cai, I. Brener, J. Lopata, J. Wynn, L. Pfeiffer, and J. Federici, "Design and performance of singular electric field terahertz photoconducting antennas," Appl. Phys. Lett. **71**(15), 2076–2078 (1997).
26. B. Heshmat, H. Pahlevaninezhad, Y. Pang, M. Masnadi-Shirazi, R. Burton Lewis, T. Tiedje, R. Gordon, and T. E. Darcie, "Nanoplasmonic terahertz photoconductive switch on GaAs," Nano Lett. **12**(12), 6255–6259 (2012).
27. O. Hatem, J. R. Freeman, J. E. Cunningham, P. J. Cannard, M. J. Robertson, E. H. Linfield, A. G. Davies, and D. G. Moodie, "Generation of Terahertz Radiation from Fe-doped InGaAsP Using 800 nm to 1550 nm Pulsed Laser Excitation," J. Infrared Millim. Terahertz Waves **37**(5), 415–425 (2016).
28. H. W. Dinges, H. Burkhard, R. Lösch, H. Nickel, and W. Schlapp, "Refractive indices of InAlAs and InGaAs / InP determined by spectroscopic ellipsometry," Appl. Surf. Sci. **54**, 477–481 (1992).
29. P. B. Johnson and R. W. Christy, "Optical constants of the noble metals," Phys. Rev. B **6**(12), 4370–4379 (1972).

1. Introduction

The development of terahertz (THz) frequency technologies has received extensive interest over the last decade, not only for the study of fundamental science [1–3], but also for applications including biomedical imaging [4], drug sensing [5], non-destructive testing [5], security screening [6] and gas spectroscopy [7]. One of the best-established sources of THz radiation is the semiconductor photoconductive emitter, which can generate both pulsed and continuous wave (CW) THz radiation depending on the optical excitation mode. Most commonly, a photoconductive emitter excited by an ultrafast femtosecond laser is employed for the generation of broadband THz radiation [8]. Nevertheless, there is considerable potential to realize compact and low-cost systems based on CW photomixers for both THz radiation generation and detection [9,10]. The improved frequency resolution and the reduced

Optics EXPRESS

system complexity that could be achieved makes such CW photomixer systems appealing for many applications.

Photomixing typically makes use of a pair of CW lasers operating in the visible or near-infrared (NIR), with a frequency difference set to the desired THz frequency. These laser fields are mixed on a semiconductor surface to produce THz radiation at the difference frequency that is then radiated through an antenna into free-space [11]. A similar process can be used to perform coherent detection using the same pair of lasers, which can lead to very high signal-to-noise ratios [12]. Compared with other THz generation and detection schemes, photomixing enables the development of compact and cost-effective systems by exploiting diode lasers, optical fibres and other optical components commonly used by the telecommunications industry. In addition to these advantages, it is also possible to achieve very high spectral resolution using photomixer systems because the linewidth of the emission is dictated by the driving diode lasers. The principal drawback though is the limited power output, particularly at higher frequencies.

Photomixer devices comprise three essential elements: a) the photoconductive material that converts the optical radiation into electronic carriers, which should ideally have short carrier lifetimes; b) the electrodes that accelerate these carriers before recapture; and, c) the antenna that couples the generated radiation into free space. The most established electrode design for CW photomixers uses interdigitated metal fingers in the active region [13]. This design allows a relatively small gap between electrodes (typically 1–2 μm), and affords a large interaction region with the incident radiation. However, since the emitted power depends on the capacitance of the active region [14] there is a trade-off, since a larger active area leads to less efficient generation.

Several methods have been investigated to improve the optical-to-THz conversion efficiency of the photomixers. These include: using resonant antennas to increase the emitted power at a particular frequency [15]; employing improved semiconductor substrates with high dark resistivity, high mobility and short carrier lifetime [16, 17]; and, improved active region designs. Of these approaches, improved active region design has recently received widespread attention. This is partly motivated by the possibility to relax the requirements on intrinsic semiconductor properties such as carrier lifetime through the use of nano-structured electrodes, an attractive proposition because of the potential broadband enhancement. This method of employing nano-structured electrodes has shown significant improvements in THz emission from photoconductive emitters excited with femtosecond lasers [18], and more recently with a pair of CW diode lasers [19]. In these studies, nano-grating (NG) electrodes based on nanometre-spaced electrodes were introduced into the active region and were found to have two beneficial effects. First, the grating improved the coupling of the incident laser beam into the semiconductor material, thus increasing the optical absorption. Second, surface plasmons tightly bound to the metal-semiconductor interface were reported to generate a higher population of electrons close to the anode thereby decreasing the transit time of the electrons. This second effect should reduce the requirement to use semiconductor materials with short carrier lifetimes [18–21]. Another photomixer design that makes use of nano-electrodes is based on ‘nanogap’ emitters, where the nanostructured anode and cathode are separated by few nanometres [22]. The generation mechanism in this case is due to an enhanced electric field at the sharp metal corners of the nanogap electrodes, which leads to an improved optical coupling resulting in improved THz power. The work

Optics EXPRESS

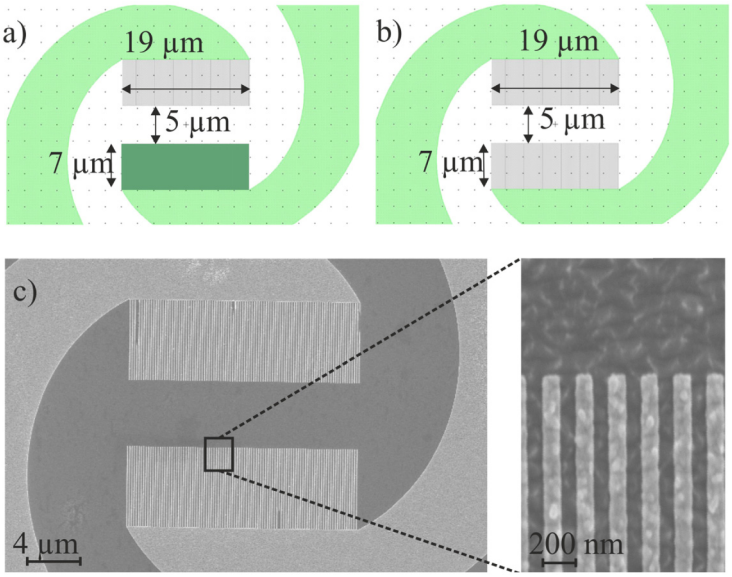

Fig. 1. Schematic layout of the active region of the (a) SSNG and (b) DSNG design with the dimensions of the active region, NG and gap marked. (c) SEM image of the fabricated DSNG design, shown together with a magnified section showing the dimensions of the active region.

of H.Tanoto *et.al* [22]. reported a factor of two enhancement in the emission using this technique, compared with an interdigitated design.

In this work, we focus on the generation mechanism behind NG electrodes and the applicability of these structures to CW THz photomixers. Two different active region designs have been compared–a single-sided nano-grating (SSNG) and a double-sided nano-grating (DSNG), as shown in Fig. 1. The SSNG has the grating on only one side of the active region with the other electrode not structured. The DSNG design has gratings on both sides of the active region. In each case, the active region designs have the same active area, are coupled to the same antenna design, and are fabricated on the same semiconductor material. The gratings consist of 100 nm-wide metal lines with a 200 nm pitch, a design that has been reported to provide enhanced absorption for both 780 nm and 1550 nm wavelength incident radiation [23]. We compare the performance of the two NG electrode designs in terms of the current-voltage characteristics and THz emission bandwidth. Furthermore, in order to understand the contribution of the NG electrodes to the THz generation mechanism, the emitters are mapped as a function of the laser excitation spot position under different bias conditions.

2. Experimental arrangement

The semiconductor material used throughout this study is Fe-doped indium gallium arsenide phosphide (Fe:$In_{0.70}Ga_{0.30}As_{0.87}P_{0.13}$) grown by metal-organic chemical vapor deposition (MOCVD), Fe-doped to a concentration of 4.0×10^{16} cm^{-3}. The molar concentration results in a semiconductor bandgap equivalent to 1550 nm; this material has been shown to provide good performance when used with active regions incorporating interdigitated fingers. The wafer growth details and processing procedures have been previously discussed in detail [17].

A two-turn self-complementary logarithmic spiral antenna with a central active area of dimensions 19 µm × 19 µm was designed using Ansys HFSS software. Figure 1 shows the schematic layout of the SSNG and DSNG incorporated in this central active area. The SSNG consists of a grating of overall dimensions 19 µm × 7 µm on one side, and a plane metal electrode of the same size on the opposite side, separated by a 5.0 µm gap. The DSNG has the same gratings (19 µm × 7 µm) on both sides of the 5.0 µm gap. The fabrication of the SSNG

Optics EXPRESS

and DSNG was carried out in two steps. The first step defined the grating along with the first turn of the spiral by electron-beam lithography. Ti/Au of thickness 5 nm/45 nm was used for metallization. The remaining spiral was then defined using a second electron-beam lithography process followed by metallization and lift-off. In this case Ti/Au with thickness 10 nm/150 nm was used. This multi-step lithography process was implemented since it was not possible to form good quality low line-edge-roughness 100 nm wide structures in 150 nm thick metal, via lift-off patterning. A scanning electron microscope (SEM) image of the DSNG design active region after fabrication is shown in Fig. 1(c) along with a high-magnification image of the nano-grating. Finally, contact pads were defined using optical lithography, with Ti/Au of thickness 10 nm/150 nm used for all devices.

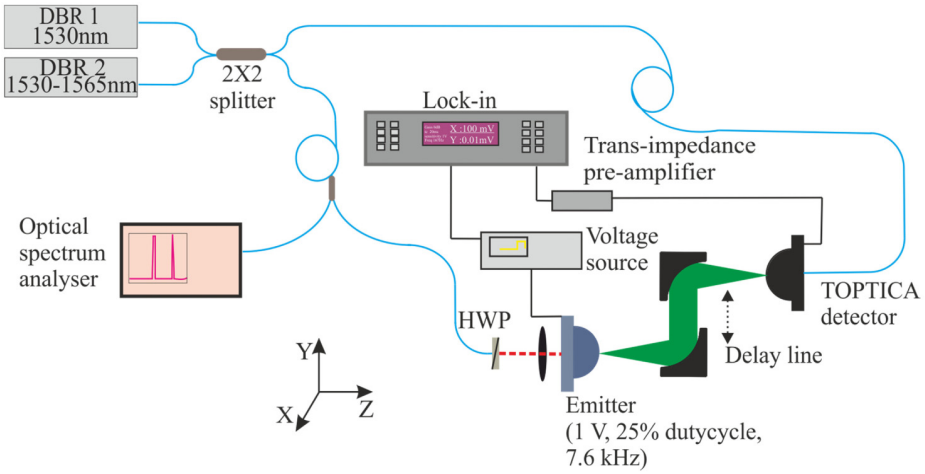

Fig. 2. Schematic diagram showing the experimental arrangement used for emitter characterization.

The experimental arrangement used for the study is shown in Fig. 2. The devices were excited by a pair of commercial, tunable distributed Bragg reflector (DBR) Oclaro Lambda FLEX iTLA TL5000 lasers operating in the telecommunications 'C-band' (1530–1565 nm). One laser (DBR1) was kept at a fixed wavelength (~1530 nm) and the other laser (DBR2) was tuned electrically. The outputs from the fibre-coupled lasers were combined and split with a polarisation-maintaining 2 × 2 fibre splitter, and an optical spectrum analyser was used to monitor the laser emission. One output from the splitter was collimated through a half-wave plate and focused by an aspheric lens onto the emitter, and had an incident power of 10 mW. The THz radiation generated was collected using a 3.0 mm-diameter hyper-hemispherical silicon lens attached to the backside of the substrate and an *f/2* parabolic mirror. This was then focused onto a fibre-coupled InGaAs coherent detector (TOPTICA Photonics, EK-000725) using a second *f/2* parabolic mirror. The second fibre output provided 13 mW of optical power to this detector. In order to enable phase control and ensure the optimum path difference between the emitter and detector, the second parabolic mirror and detector were placed on a mechanical delay line. The current generated in the detector was amplified using a FEMTO trans-impedance amplifier with a gain of 10^7 (V/A) and measured using a lock-in amplifier referenced to the applied bias on the grating at 7.6 kHz.

3. Results

Figure 3(a) shows the photocurrent measured in the SSNG and DSNG emitters as a function of applied bias at 10 mW incident laser power. For these measurements a low DC bias (corresponding to an applied field of up to 0.2 kV/cm), was applied to prevent damage to the emitters by excessive heating. The photocurrent in the SSNG emitter was found to be slightly

Optics EXPRESS

smaller than the DSNG emitter, which could be due to the enhanced absorption induced by the additional grating structure on the DSNG device. Both devices showed very low dark current, as expected from the Fe:InGaAsP material [17], measured to be less than 5 μA at 0.1 V.

For measurement of the THz output, the devices were biased with + 1 V pulses at a frequency of 7.6 kHz and a 25% duty cycle. In the case of the asymmetric SSNG device, the grating was positively biased, with the plane electrode grounded. The 25% duty cycle was chosen to reduce the risk of damage after some devices were damaged when a 50% duty cycle was applied. Figure 3(b) shows the THz field amplitude measured from the two emitter designs as a function of laser difference frequency in the range 100−2000 GHz. The bandwidths, defined as the frequency at which the signal drops below the noise floor, are found to be ~2 THz and ~1.6 THz for the SSNG and DSNG devices, respectively. This detection bandwidth is less than what was measured for a similar device with an interdigitated active region (2.4 THz) using the same experimental arrangement [17]. The THz amplitudes are similar for the SSNG and DSNG devices at low frequencies, whereas the SSNG device slightly outperformed the DSNG emitter at higher frequencies. The reason for this difference is not clear.

It is worth noting that the emission bandwidths and powers measured here for both the NG devices are lower than those measured from an interdigitated device on the same material [17]. While this previously reported interdigitated device had a slightly different antenna design, which can result in a 3 dB difference in output power at 2 THz, this does not account for the greater bandwidth (~2.4 THz) observed compared to our NG devices. Furthermore, the peak output powers for the DSNG and SSNG devices, measured using a calibrated bolometer, are 10.8 nW and 26 nW at 1 THz, respectively. These are comparatively lower than the 60 nW peak power measured previously for the interdigitated device on the same material [17]. For the optical powers used in the study, the emitters were operating close to saturation, with an approximately linear dependence of THz power on optical power. We have also compared the maximum expected output powers, calculated from the photocurrent at zero frequency [24]. This predicts an upper bound on the power of 240 nW at 1 THz for both the NG device designs, assuming a photocurrent of 0.4 mA, an antenna radiation resistance of 72 Ω, an active region capacitance of 0.5 fF, and a carrier lifetime of 0.75 ps. Comparing this with the performance of the interdigitated devices fabricated on the same wafer, our results suggest that there is no significant reduction in the effective carrier lifetime, below the material carrier lifetime, for the SSNG and DSNG devices, that has been suggested for this type of design [19]. Compared with the work of S.H.Yang *et al.* [20], which makes use of the same grating structure and similar antenna design, the lower powers measured here are partly explained by the lower photocurrent. However, if the same procedure for estimating the power based on the photocurrent that we perform here is performed for the data given by S.H.Yang *et al.* [20], extremely high collection efficiencies are found, which could be responsible for the reported enhanced power levels.

Optics EXPRESS

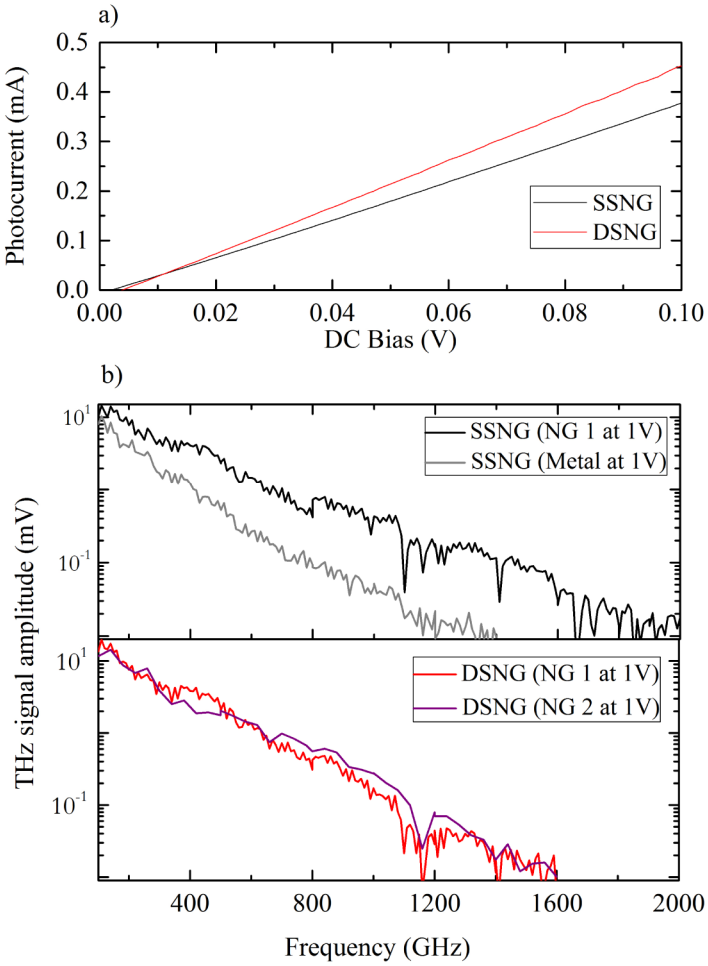

Fig. 3. (a) Photocurrent measurement from the DSNG and SSNG emitters as a function of DC bias at an incident optical power of 10 mW. (b) THz amplitude as a function of laser beat frequency from the two different designs, SSNG (top) and DSNG (bottom), at different bias orientations. For the SSNG, black and grey curves represent the bandwidth scan performed when the NG and plane metal electrode was biased, respectively. For the DSNG, red and purple curve represents the same measurements with the NG1 and NG2 biased, respectively.

Figure 3(b) shows the THz field amplitude measured from the SSNG and DSNG devices when biased in reverse polarity, i.e. with the 1 V bias applied to the plane metal electrode of the SSNG device. For the DSNG device, there was no measureable change in the emission characteristics, which is expected since the electrodes are symmetric. For the asymmetric SSNG device, however, switching the bias resulted in a significant decrease in signal. This suggests that there is an enhanced THz emission only when the positively-charged anode is structured as a nano-grating. Indeed, the importance of the anode is well known in photoconductive THz generation; the photo-generated electrons are collected by the anode, and since the mobility of electrons is significantly higher than the holes, electrons are the dominant carrier for THz generation.

While this indicates the importance of the nano-grating, it does not explain the generation mechanism. To gain insight into this, we mapped the THz emission as a function of laser excitation position. The sample was raster scanned in the X-Y plane (perpendicular to the excitation direction) with the laser spot remaining stationary, using a motorized stage to move the sample along the X-axis, with the position in the Y-direction adjusted manually. The scan

Optics EXPRESS

resolution was 0.9 µm and 1.0 µm in the X- and Y-directions, respectively. It was confirmed that this small movement (~30 µm) of the sample did not affect the collection efficiency. The laser beam was focussed to a spot size of ~6 µm using a microscope objective, and the laser was horizontally polarized, perpendicular to the metal grating.

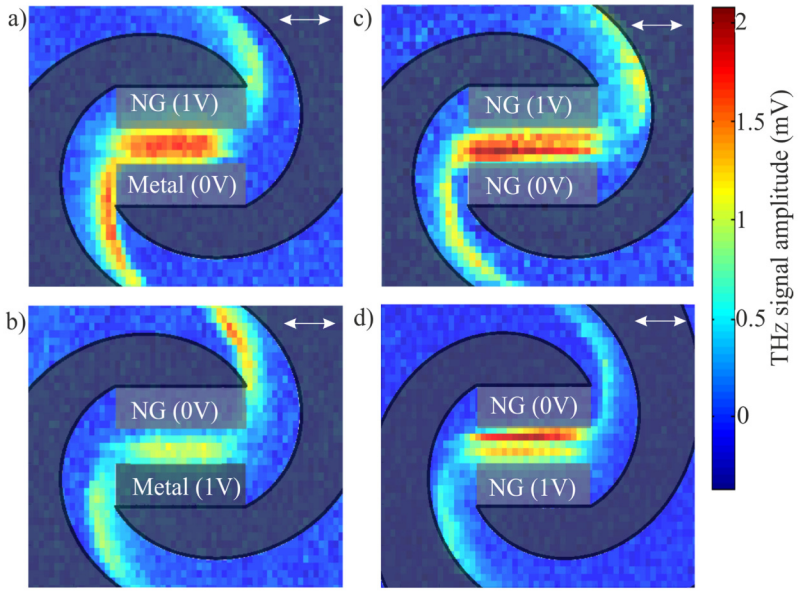

Fig. 4. Raster scanned images showing the THz amplitude as a function of the laser exciting position for the SSNG and DSNG emitters at 510 GHz. In each case, the appropriate electrode is biased at 1 V, with a 25% duty cycle at 7.6 kHz. An image of the two-turn log-spiral antenna design is overlayed on the data to aid understanding. The SSNG design with (a) the NG biased and (b) the plane metal electrode biased. The DSNG design with (c) the first NG biased and (d) the second NG biased. The polarization direction of the incident laser is shown in the top right corner of each image.

Figure 4 shows maps of the THz signal at 510 GHz as a function of laser beam excitation position for the SSNG and DSNG emitters with different bias polarities. The maximum amplitude is obtained when the laser ~6 µm spot excitation is positioned in, and fills, the gap between the two electrodes, for both the SSNG and DSNG devices, Figs. 4(a)-4(d). Furthermore there is no significant emission when the excitation is positioned on the centre of one of the NG electrodes. This observation is not in agreement with previous work in which it has been proposed that excitation in the centre of the NG electrodes should excite surface plasmons and result in the greatest THz emission [20]. When the bias direction was switched, the DSNG emitter, Figs. 4(c) and 4(d), maintained the same maximum power level, and a small change in the excitation position corresponding to this maximum signal was observed. For the SSNG device, Figs. 4(a) and 4(b), reversing the bias caused a significant reduction in THz amplitude (~40%), as discussed above, but the excitation position corresponding to the greatest amplitude did not change significantly. This same mapping procedure was performed at both higher (810 GHz) and lower (210 GHz) frequencies and showed qualitatively the same behaviour. Our data indicates that the THz generation mechanism in these devices appears to be associated with the tips of the nano-grating electrodes rather than the centre of the grating structure. This suggests that the tips on the anode grating cause an enhanced concentration of the laser electric field at the sharp corners of the electrodes, resulting in higher absorption in this region, leading to higher numbers of photoelectrons and enhanced THz emission. The is also expected to be a concentration of the electrostatic field (applied bias) at these sharp tips. This effect is well known for THz generation [25] in dipole emitters,

Optics EXPRESS

and has been used more recently with plasmonic enhancement [26]. In the case of the SSNG device, when the plane metal is positively biased, no enhanced output power is observed because there are no sharp tips present.

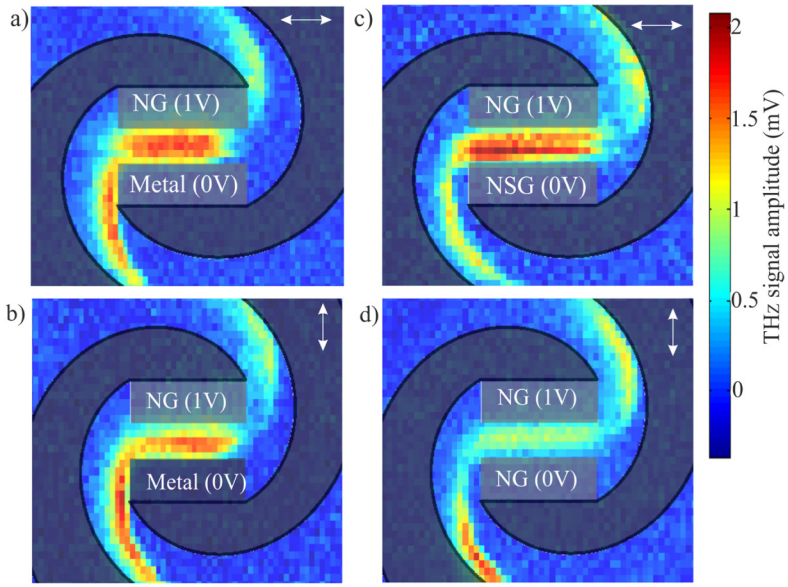

Fig. 5. Raster scanned images showing the THz amplitude as a function of the laser exciting position for the SSNG and DSNG emitter design, for two orthogonal incident laser polarizations at 510 GHz. In each case, the appropriate electrode is biased at 1 V, with a 25% duty cycle at 7.6 kHz. An image of the two-turn log-spiral antenna design is overlayed on the data to aid understanding. The SSNG design with (a) horizontal and (b) vertical polarizations; the DSNG design with (c) horizontal and (d) vertical polarizations.

Mapping was also carried out for the orthogonal laser polarisation, with the electric field polarised vertically, i.e. parallel to the metal fingers of the grating as shown in Figs. 5(a)-5(d). It was found that the DSNG device experienced ~70% reduction in THz amplitude, whereas the SSNG device showed only ~30% decrease in amplitude, compared to the horizontal polarisation. In both cases, the decrease in amplitude with vertically polarized light is due to the gratings acting as a wire-grid polarizer that reflects the incident radiation. The smaller change observed in the SSNG device is consistent with this effect as there is only one NG. In all cases, however, the THz signal was highest with the excitation centred in the gap between the electrodes. Similar investigations were performed with different grating periods between 200 nm–400 nm and the results were similar.

The THz generation mechanism in these devices has also been studied with pulsed excitation, with the mapping procedure repeated in a THz time-domain spectroscopy system. For these measurements the emitters were excited with 95 fs pulses, centred at 780 nm, and an incident laser power of 20 mW, from a TOPTICA fibre Pro laser. We note that this material has previously been characterized for THz emission across a range of wavelengths in the range 800−1550 nm [27]. A 1.0 mm-thick ZnTe crystal, a λ/4 plate, Wollaston prism and a New Focus Nirvana balanced photodiode were used for electro-optic sampling of the THz emission in the time domain. The 20 mW laser pulse was focused on to the active area using the same 20 × objective lens as used above, but in this case the spot size was larger, ~13 μm due to chromatic aberration. The emitters were biased in the same way as previously. Figure 6 shows the pulsed mapping data obtained from the SSNG and DSNG devices, which reveals the same behaviour as found above for CW excitation; the greatest power was detected when the excitation was focused at the centre of the gap, between the electrodes. Figure 6(c) shows

Optics EXPRESS

the time domain waveform measured from different parts of the active region, corresponding to points on the inset image. The THz electric field amplitude maximum occurred at the same optical delay position.

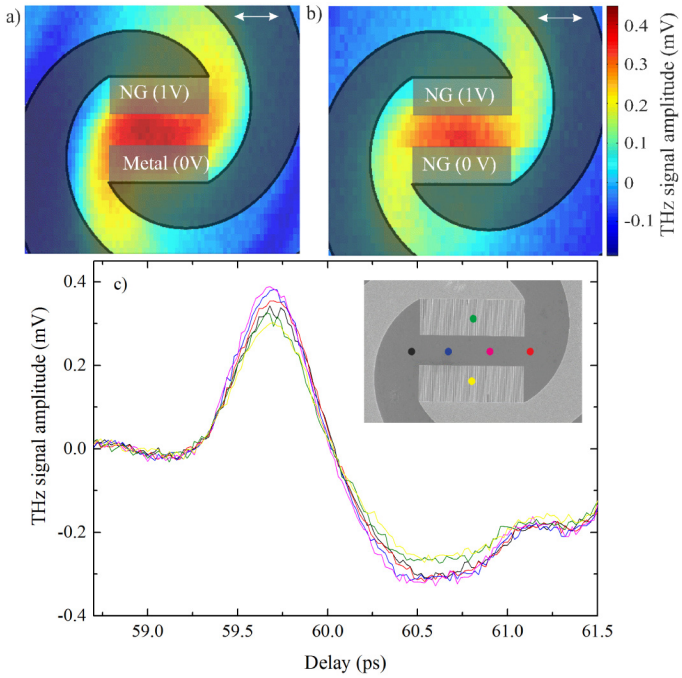

Fig. 6. Raster scanned images showing the peak THz amplitude as a function of excitation position for (a) the SSNG, and (b) the DSNG emitter design, respectively, obtained through THz time-domain spectroscopy. In each case, the appropriate electrode is biased at 1 V, with a 25% duty cycle at 7.6 kHz. An image of the two-turn log-spiral antenna design is overlayed on the data to aid understanding. The spotsize is larger compared to the CW mapping measurements owing to the chromatic aberration of the lens. (c) Measured THz time domain waveforms for different laser excitation positions. Inset shows the corresponding to the laser excitation positions

4. Simulations

To confirm our interpretation of the results, we have also performed full-wave electromagnetic simulations of the devices and optical excitation using the commercially available software package *CST studio suite*. The model geometry is shown in Fig. 7(a), and shows the gold electrodes in yellow and the InGaAsP absorption layer in blue. Values for the complex index in this material were approximated to be the same as InGaAs lattice matched to InP [28] and the complex index for the gold electrodes was taken from P. B. Johnson *et al.* [29].

Optics EXPRESS

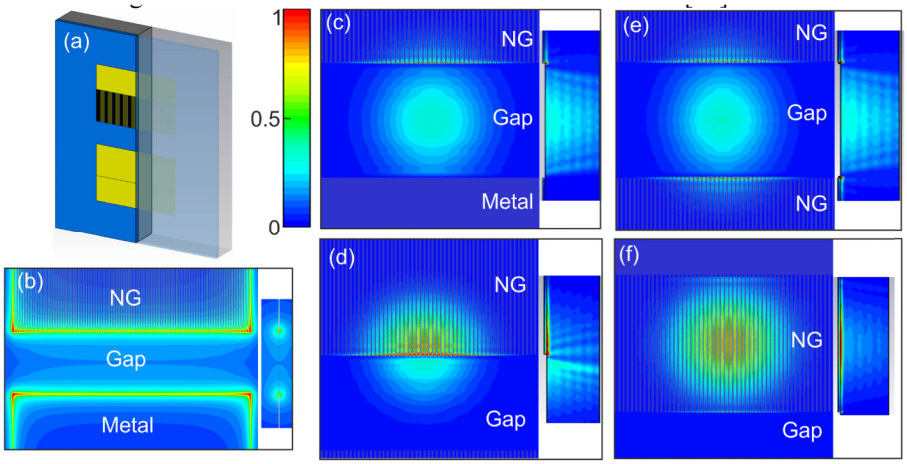

Fig. 7. Results for full-wave simulations of DSNG and SSNG devices. (a) Diagram of 3-dimentional model showing the SSNG device with electrodes in yellow and semiconductor layer in blue. (b) Top view and corresponding cross-section of the calculated electrostatic field magnitude for SSNG device, showing electric field 25 nm below the gold electrodes surface. (c)-(f) Top-views and corresponding cross-sections of absorption power density in the semiconductor material 25 nm below the gold electrodes. The cross-sections are taken along the edge of the central grating bar. (c) SSNG device, spot focused in the gap, (d) DSNG device, focused on tips, (e) DSNG device, focused in gap, (f) DSNG device focused on grating.

Figure 7(b) show the electrostatic field applied to the active region in top-view and cross-section. As expected it shows that the strongest electrostatic field is located at the tips of the grating and the edge of the plane metal, while the field beneth the plane metal and grating is relatively weak. There is also some local enchancement at the tips of the grating, although the 'average' along the plane metal edge and grating edge is the same.

To simulate the NIR excitation, an electromagnetic wave with a wavelength of 1550 nm, shaped as a Gaussian beam, with a width of 6 μm, is launched from the top of the air region and impinges on the active area. This simulation has been performed for wavelengths across the C-band (1530 nm–1565 nm) however very little dependence on wavelength was observed for either absorption in the InGaAsP layer, or loss in the Gold layer. The results, Figs. 7(c)-7(f), show the optical absorption in the DSNG and SSNG structures for different positions of laser spot excitation. Each figure shows a 'top view' and, right, a cross-section into the device layers, across the gap. The top-view is shown 25 nm below the electrodes, the cross-section is shown along the edge of a grating bar. Figure 7(c) shows the beam focused in the center of the gap for the SSNG device and highlights the role of the grating tips in enchancing optical absorption near the electrode, and in particular the anode; there is significantly more optical absorption at the grating tips compared to the plane metal egde. The highest *total* absorption in the semiconductor is found for the DSNG device with beam centered in the gap Fig. 7(e), where there is no grating covering this region. However, within the upper 50 nm of the active material, the absorption is highest when the beam is centered on either the tips, Fig. 7(d) or the grating Fig. 7(f). The calculated absorption is similar for these two cases, with the spot on the grating, Fig. 7(f), showing slightly higher absorption. However, since the electrostatic field underneth the grating is small the THz generation here will be small. If one considers this calculated absorption together with the calculation of the electrostatic field, the highest currents (and hence highest THz fields) will be generated when the laser excitation is close to the tips. Here there is an enhancement of both the electrostatic field and the NIR excitation generating carriers close to the electrode, supporting the experimental interpretation.

Optics EXPRESS

This detailed study has examined the applicability of using photomixers incorporating nano-gratings for CW THz emission with ~1550 nm excitation. Results from experiments and simulations indicate that the generation mechanism in the nano-gratings is enhanced by the concentrated optical electric field at the tips of the grating on the anode. This results in a higher concentration of photoelectrons close to the anode, which when accelerated by the applied electric field, leads to enhanced THz emission. This is different to the conclusion of some recent work that suggests a plasmonic enhancement effect, for which the excitation should be centred on the middle of the grating for maximum THz emission. By comparing different emitter designs we have found that nano-structuring of the anode results in higher THz emission power, however, the overall performance in terms of emitted THz power and bandwidth is lower for nano-structured electrode devices compared to interdigitated devices with 2–5 pairs of fingers. Future designs for high power CW THz emission could combine the long interaction length of conventional interdigitated fingers with nano-structuring of the electrode fingers.

Funding

This work was supported by the Engineering and Physical Sciences Research Council [EP/J017671/1, "COTS" and EP/J002356/1]. Funding was also received from the European Community's Seventh Framework Programme [FP7-IDEAS-ERC] under Grant Agreement No. 247375 "TOSCA." Support from the Royal Society and Wolfson Foundation (A.G.D. and E.H.L.) is also acknowledged. The data associated with this paper are openly available from the University of Leeds data repository http://doi.org/10.5518/132.